Derivatives of two-dimensional MXene-MOFs heterostructure for boosting peroxymonosulfate activation: Enhanced performance and synergistic mechanism

Xin Guo, Hao Zhang, Yiyuan Yao, Chengming Xiao, Xin Yan, Ke Chen, Junwen Qi, Yujun Zhou, Zhigao Zhu, Xiuyun Sun, Jiansheng Li[*]

Jiangsu Key Laboratory of Chemical Pollution Control and Resources Reuse, School of Environmental and Biological Engineering, Nanjing University of Science & Technology, Nanjing 210094, China

ABSTRACT

Integrating the merits of the substrate and active sites with the water matrix is of significant importance to design novel catalysts for peroxymonosulfate (PMS)-based advanced oxidation processes. A sandwich-like heterostructure catalyst (MCoO@Co-N-C) were fabricated via anchoring zero-dimensional metal-organic frameworks (MOFs)-derived CoO nanoparticles on two-dimensional $Ti_3C_2T_x$ MXene nanosheets. Benefiting from the distinctive structure, the resultant catalysts achieved excellent decontamination performance under high salinity conditions (200 mM). Nearly 100% efficiency of bisphenol A (BPA) was degraded within 10 min only using 0.05 g L^{-1} catalyst and 0.1 g L^{-1} PMS, with exceptional high turnover frequency (TOF) value (8.64 min^{-1}) which was 22.5 times higher than that of MOFs derived catalysts without MXene. A mediated-electron transfer mechanism is found to be conducive to the oxidation of BPA. This work provides a new approach to novel catalysts designed for removing trace organic contaminants (TrOCs) in saline water.

1. Introduction

Peroxymonosulfate-based advanced oxidation processes (PMS-AOPs) have recently received huge attention in the degradation of trace organic contaminants (TrOCs) [1,2]. PMS-AOPs primarily oxidize organic pollutants by reactive oxygen species (ROS) produced via either free radicals that comprise sulfate radical (SO$_4^{\bullet-}$) [3], hydroxyl radical ($^{\bullet}$OH) [4], and superoxide radical (O$_2^{\bullet-}$) [5] or nonradical pathways which includes singlet oxygen (^{1}O$_2$) [6], high-valence metal induced oxidation [7], and electron-transfer processes (ETP) [8]. As for radical-based AOPs, the coexisting inorganic ions remain a great challenge for practical wastewater. These ions (e.g., Cl$^-$, HCO$_3^{2-}$, NO$_3^-$) can rapidly react with the oxidative species (SO$_4^{\bullet-}$/$^{\bullet}$OH), adversely affecting the degradation performance of the target contaminants and forming hazardous halogenated by-products [9,10]. Moreover, the inhibition effects seriously limit the practical application for repairing organic wastewater under high salinity conditions. Undoubtedly, a suitable degradation pathway in saline wastewater should be necessary to find.

Nonradical-based AOPs have been investigated for alleviating the inhibitory effects of reactions in the radicals and inorganic ions [11]. Especially, ETP has garnered extensive attention owing to plenty of technical advantages. For instance, (i) ETP has high selectivity for electron-rich organic pollutants [12]; (ii) A lower consumption of persulfate has been confirmed during ETP, thus significantly reducing the amount of oxidant input [13]; (iii) ETP can still maintain its excellent efficiency within a wider pH range and would not generate hazardous halogenated by-products even under the presence of inorganic anions [14]. Based on the above superiority, ETP displays a wide application in PMS-AOPs. Various carbonaceous materials, including N-CNTs [15], graphited nanodiamond [16], and several metal-based catalysts such as CuO [17] and amorphous MnO$_2$ [18] have been reported to trigger ETP during the activation of persulfate. However, the mass-transfer rate and performance of these catalysts remain far from satisfactory. Rational design of novel catalysts with intrinsic capacity for rapid electron transfer is of significant importance, but has rarely been touched.

The unique porous structure and structural diversity of metal-organic frameworks (MOFs) make them excellent precursors and templates to fabricate nanomaterials in PMS-AOPs [19,20]. However,

individual MOFs tend to cluster into nanoparticles (NPs) during the carbonization process, resulting in a slower mass transfer and a significant reduction in catalytic activity [21]. Consequently, it is essential to stabilize MOFs on an appropriate substrate to accomplish uniform dispersion and optimized performance. MXene, possessing outstanding conductivity, abundant surface functional groups, and excellent mechanical flexibility, demonstrates superior capability in energy storage [22], sensors [23], catalysis [24], etc. The hybridization of MOFs and MXene in electrochemical applications, such as $Ti_3C_2T_x$-CoBDC [25], (CoS NP@NHC)@MXene [26], and CoZn-Se@N-MX [27], has confirmed to favor the rapid formation of charge transfer channels via strong synergistic effect. Accordingly, derivatives of two-dimensional (2D) electrically conductive MXene-MOFs heterostructure are anticipated to achieve further enhanced performance during the activation of PMS, which is allowed rapid electron transport in ETP.

In this study, a sandwich-like heterostructure catalyst (MCoO@Co-N-C) was fabricated by self-assembly of zero-dimensional (0D) MOFs on MXene nanosheets, followed by a pyrolysis strategy (Scheme 1). The resultant MXene-MOFs heterostructure derivatives successfully anchored nanosized CoO encapsulated inside the Co, N co-doped carbon shell on MXene. The open sandwich-like structure with 0D nanosized CoO@Co-N-C evenly distributed on both sides of 2D MXene plane ensures the expedited mass transfer and maximally employs each active site, effectively boosting PMS activation. Bisphenol A (BPA), a typical TrOCs, is targeted to investigate the impact of inorganic ions on the MCoO@Co-N-C system under high salinity conditions. The critical role of Co-N species was further corroborated by the element mapping analysis, X-ray photoelectron spectroscopy (XPS), and density functional theory (DFT) calculations. Additionally, to elucidate the activation mechanism of PMS, a series of explorations involving quenching experiments, electron paramagnetic resonance (EPR) detection, in situ Raman, electrochemical analysis, and DFT calculations were carried out. The study advances a newly mechanistic insight into the synergistic effect of MXene and MOFs in environmental fields during PMS-AOPs.

2. Experimental methods

2.1. Chemicals and reagents

Titanium aluminum carbide (Ti_3AlC_2, 400 mesh) was purchased from the 11 Technology Co., Ltd. (Changchun, China). Oxone (KHSO$_5$•0.5KHSO$_4$•0.5 K$_2$SO$_4$), zinc nitrate hexahydrate (Zn(NO$_3$)$_2$•6 H$_2$O), L-histidine, and bisphenol A (BPA) were bought from Sigma-Aldrich (MO, USA). 2,2,6,6- tetramethyl-4-piperidinyl (TEMP), lithium fluoride (LiF), and sodium persulfate (Na$_2$S$_2$O$_3$) were provided by Meryer (Shanghai, China). Hydrochloric acid (HCl), methanol (MeOH), and p-benzoquinone (*p*-BQ) were obtained from Sinopharm (Beijing, China). Cobalt nitrate hexahydrate (Co(NO$_3$)$_2$•6 H$_2$O), dimethyl sulfoxide (DMSO), 2-methylimidazole (2-MeIm), *tert*-butyl alcohol (TBA), potassium dichromate (K$_2$Cr$_2$O$_7$), and sodium

perchlorate (NaClO$_4$) were purchased from Aladdin (Shanghai, China). Deionized (DI) water was supplied by the Millipore Milli-Q purification system. All of the chemicals were employed without further purification.
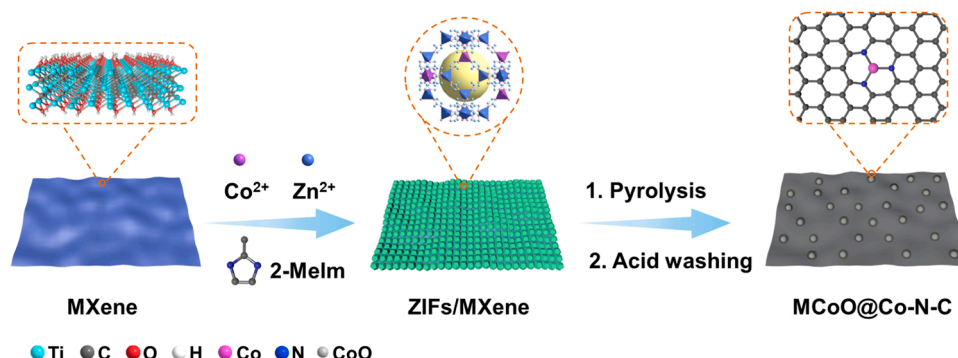
2.2. Synthesis of MCoO@Co-N-C

The few-layered $Ti_3C_2T_x$ MXene colloidal aqueous solution (2.5 g L^{-1}) was obtained via slightly modified based on the previous study [28] in which the amounts of LiF and HCl were changed to 1.6 g and 20 mL 12 M, respectively. To synthesize zeolitic imidazolate frameworks/MXene (ZIFs/MXene), 56 mg Co(NO$_3$)$_2$•6 H$_2$O and 244 mg Zn(NO$_3$)$_2$•6 H$_2$O dissolved in 80 mL MeOH with sonicating 5 min were added into 20 mL MXene solution, followed by sonicating for 10 min. The above solution was then quickly mixed with 80 mL MeOH solution containing 1 g 2-MeIm for 6 h under stirring at room temperature. The obtained products were centrifuged and washed several times with MeOH to collect it. Finally, ZIFs/MXene was obtained by drying in a vacuum oven. For comparison, ZIFs were synthesized by the same methods without adding MXene, ZIFs/GO were prepared by replacing MXene with graphene oxide (GO). Finally, MCoO@Co-N-C was prepared by directly calcinating at 900 °C (2.5 °C min^{-1}) for 2 h under the N$_2$ flow. The redundant cobalt species were removed by acid washing. Similarly, ZIFs-900, MXene-900, and ZIFs/GO-900 were prepared by pyrolysis of ZIFs, MXene, and ZIFs/GO as a precursor respectively via the same procedure. Besides, to obtain catalysts loaded with different ZIFs, the mass ratios of metal salts (Co(NO$_3$)$_2$•6 H$_2$O and Zn (NO$_3$)$_2$•6 H$_2$O) to MXene were 8, 6 and 4. These catalysts were labeled as MCoO@Co-N-C-8, MCoO@Co-N-C and MCoO@Co-N-C-4, respectively.

2.3. Experimental procedure

All of the BPA degradation tests were performed at room temperature (25 °C) by a 100 mL glass beaker consisting of 0.05 g L^{-1} catalyst, 0.1 g L^{-1} PMS, and 20 mg L^{-1} BPA. In a typical experiment, 5 mg catalysts were dispersed into a 100 mL BPA solution with 1 min ultrasonic dispersion. After stirring for 20 min, the adsorption-desorption equilibrium was established. Then, with the addition of 10 mg PMS to trigger the reaction, 0.75 mL of the solution was taken out and 0.75 mL Na$_2$S$_2$O$_3$ (100 mM) was added to terminate the reaction at selected time intervals. The mixture was filtered through a 0.45 μm glass fiber filter and detected via high-performance liquid chromatography (HPLC) for further analysis.

2.4. Characterizations and analytic methods

The structure and surface morphology of the samples was performed on scanning electron microscopy (SEM, JEOL 7800) and transmission electron microscopy (TEM, JEM 2100 F) respectively. The microstructure of samples was evaluated by the Bruker D8 at 40 kV and 40 mA by

Co^{2+} **Zn^{2+}**

2-MeIm

1. Pyrolysis

2. Acid washing

MXene **ZIFs/MXene** **MCoO@Co-N-C**

● Ti ● C ● O ○ H ● Co ● N ● CoO

Scheme 1. Synthetic route illustration of the MCoO@Co-N-C catalyst.

X-ray diffraction (XRD, Cu Kα, λ = 1.5418 Å). An FT-IR spectrometer (Bruker HYPERION, Germany) was used to measure the chemical groups on the catalyst surface. N_2 adsorption-desorption isotherms were recorded at 77 K using Micromeritics ASAP-2020. The analysis of XPS was obtained by a photoelectron spectrometer (PHI Quantera II System). Residual BPA was quantified by high-performance liquid chromatography (HPLC, Waters e2695) equipped with a 2998 PDA detector and a C-18 column. The ratio of the mobile phase (MeOH/water) was 7/3 with a 1.0 mL min^{-1} flow rate. To identify the degradation pathway of BPA, liquid chromatography-tandem mass spectrometry (LC-MS/MS, AB SCIEX TripleTOF™5600 +, USA) was used to detect the intermediates of degradation products. The measurement of electron paramagnetic resonance (EPR, Bruker A300, Germany) was used to identify ROS with different spin-trapping agents. The zeta potential of the samples was assessed by the zeta potential analyzer (ZetaPALS, Brookhaven Instruments Co., USA). Electrochemical experiments such as electrochemical impedance spectroscopy (EIS), chronoamperometry as well as linear sweep voltammetry were carried out on a CHI 760D electrochemical workstation. The cobalt leaching concentration was determined by inductively coupled plasma emission spectrometer (ICP-OES, Thermo Fisher Scientific, iCAP PRO). The total organic carbon (TOC) was analyzed using a TOC analyzer (vario TOC, Elementar, Germany). The kinetic rate constant (k) of BPA degradation followed the first-order kinetic model, which was calculated based on Eq. (1):

$$ln\frac{C_t}{C_0} = -kt \tag{1}$$

where C_0 was the initial concentration, and C_t was the concentration at a given time (t).

3. Results and discussion

3.1. Characterization of the catalysts

The SEM image of ZIFs/MXene showed that the uniform MXene nanosheets were covered with ultrasmall ZIFs NPs (Fig. 1a). The ZIFs NPs with the ultrasmall diameter (approximately 40 nm) were aggregated together and almost fully coated on both sides of the MXene nanosheets in the high magnification SEM image (Fig. 1b). The formation of this MXene-MOFs heterostructure is due to the negatively charged MXene with a zeta potential of − 39.7 mV [29] absorbing positively charged Co^{2+} through electrostatic interaction, followed by the surface-anchored Co^{2+} coordinating with 2-MeIm. Such a sandwich-like heterostructure can produce a large number of high-density active sites, accelerating the mass transfer process and increasing the catalytic reaction rate. After subsequent calcination in N_2, the detailed morphology and structure of as-synthesized MCoO@Co-N-C were examined by SEM and TEM. As displayed in Fig. 1c and d, evenly dispersed ZIFs on MXene underwent chemical transformation to form CoO NPs enclosed in Co-N co-doped carbon shells. The selected area electron diffraction (SAED) image (Fig. 1e) illustrated continuous diffraction rings corresponding to the crystal planes of graphite carbon and CoO NPs, respectively [30]. Moreover, the high-resolution TEM (HRTEM) pattern of the sample (Fig. 1f) revealed that CoO NPs were encapsulated in the graphite carbon shells. The high-resolution lattice spacings of 0.246 and 0.340 nm are attributed to the (111) facet of CoO as well as the (002) facet of graphite carbon [31], which is correspondent with the SAED result. The element mapping analysis in Fig. 1g presented that Ti, C, N, Co, and O elements authenticated the distribution throughout the entire MXene nanosheets. Moreover, the overlap of
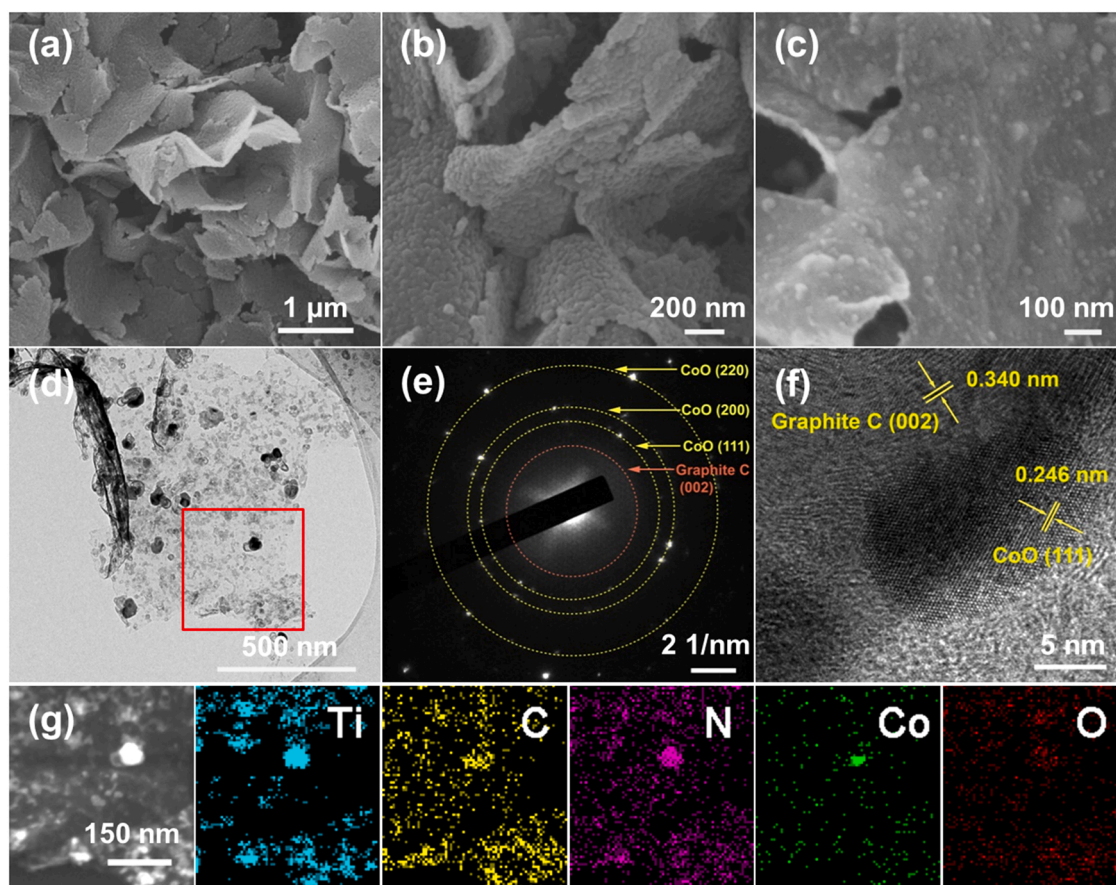

Fig. 1. SEM images of (a) ZIFs/MXene, (b) enlarged ZIFs/MXene, and (c) MCoO@Co-N-C; (d) TEM images of MCoO@Co-N-C; (e) SAED diffraction patterns of MCoO@Co-N-C; (f) HRTEM images of MCoO@Co-N-C, and (g) the relating elemental (Ti, C, N, Co, O) mapping images.

Co and N elements further verifies Co-N species in the as-obtained MCoO@Co-N-C structure, which fits well in the selected area.

From the XRD patterns of bulk Ti_3AlC_2 crystals and the exfoliated $Ti_3C_2T_x$ MXene nanosheets (Fig. S1a), the (104) peak at $2\theta = 39°$ of Ti_3AlC_2 was absent in the $Ti_3C_2T_x$ pattern, proving the successful etching of Al layers [25]. Besides, the strong diffraction peak of the (002) planes from $Ti_3C_2T_x$ compared to the original Ti_3AlC_2 had an angular offset from 9.3° to 4.6°, indicating the preparation of few-layered MXene [32]. The successful assembly of ZIFs and ZIFs/MXene was further validated by XRD analysis in Fig. S1b. To further verify the formation of ZIFs/MXene, the FT-IR spectrum of MXene, ZIFs, and ZIFs/MXene were also characterized. As shown in Fig. S2, MXene exhibited a hydroxyl group absorption vibration peak [33]. The peaks at 3143 and 1585 cm^{-1} in the FT-IR spectra of ZIFs were separately attributed to C-H bonds and C=N stretch of 2-MeIm and other complex bands in 600–1500 cm^{-1} corresponded to the stretching and bending modes of 2-MeIm [34]. These peaks were also observed in the spectrum of ZIFs/MXene, indicating that ZIFs were synthesized successfully in the presence of MXene. As exhibited in Fig. 2a, The characteristic peak at 6.6° (002) of MXene-900 and MCoO@Co-N-C were still present, indicating that MXene was not affected during the pyrolysis. It is noteworthy that the direct pyrolysis of ZIFs produced crystalline metallic Co NPs with characteristic peaks at 44.2° and 51.5° corresponding to (111) and (200) lattice planes (PDF#15–0806) [6]. After loading on MXene, MCoO@Co-N-C with diffraction peaks at 36.5°, 42.4°, 61.5°, 73.7°, and 77.5° separately representing (111), (200), (220), (311), (222) planes (PDF#43–1004) were consistent with the phase of CoO [35]. The valence change of Co may be due to the coordination of the Co ions and the surface oxygen-containing groups of MXene. The Raman spectrum was used to study the degree of graphitization. All samples displayed two distinct peaks at 1357 and 1587 cm^{-1}, corresponding to the D-band and G-band, respectively (Fig. 2b). As reported by previous literature [36], the D-band is relevant to disorders/defects of carbon materials, while the G-band is a signature for the sp^2 site in graphite carbon. The

peak intensity ratio of the D-band and G-band (I_D/I_G) is frequently used to assess the degree of graphitization. The value of I_D/I_G MCoO@Co-N-C was 0.94, which displayed that MCoO@Co-N-C had a relatively high degree of graphitization. This may be attributed to the in situ repair of the defective sites of MXene by MOFs derived carbon during the pyrolysis process. The specific surface area and pore structure of as-prepared catalysts were given in Fig. 2c. The pure ZIFs-900 whose specific surface area was 128.4 m^2 g^{-1} had a pore volume of 0.45 cm^3 g^{-1} (Table S1). After being loaded on MXene, the Brunauer-Emmett-Teller (BET) surface area of MCoO@Co-N-C increased to 310.2 m^2 g^{-1}, which was approximately 25 times that of MXene-900 (12.4 m^2 g^{-1}). This is because MXene provides robust support to prevent metal particles from aggregating, thus maximizing the exposure of the porous surface of the catalyst [25]. Additionally, the existence of obvious hysteresis loops in the MCoO@Co-N-C isotherms indicated the presence of mesopores and macropores which could also be seen in the pore size distribution inset of Fig. 2c. As stated in the IUPAC classification, the N_2 adsorption-desorption isotherms of MCoO@Co-N-C showed type IV [37]. Higher specific surface area can give more active sites for composite catalysts, implying that MXene can significantly promote ZIFs dispersion, resulting in more active sites.

XPS is usually employed to investigate the chemical status of elements. The survey XPS spectra (Fig. 2d) demonstrated typical peaks of Ti, C, N, Co, and O derived from MXene-900, ZIFs-900, and MCoO@Co-N-C. Specifically, high-resolution Co 2p spectra acquired from ZIFs-900 and MCoO@Co-N-C were shown in Fig. 3a. In the XPS spectrum of MCoO@Co-N-C, there were two main species of Co^{2+} (781.1/797.0 eV) and Co^{3+} (779.9/795.2 eV) in addition to satellite peaks (786.5/ 799.6 eV) [38]. Notably, the disappearance of Co^0 and increase of Co^{2+} in the XPS spectra of MCoO@Co-N-C were matching well the results of XRD. Moreover, as shown in Fig. S3, except for three dominant states of O-C=O (531.5 eV), -OH (532.2 eV) and H_2O_{ads} (533.0 eV), an evident peak at 530.2 eV ascribed to M-O (Co-O or Ti-O) also appeared in the O 1 s spectrum [39]. These results collectively illustrate the cross-linking
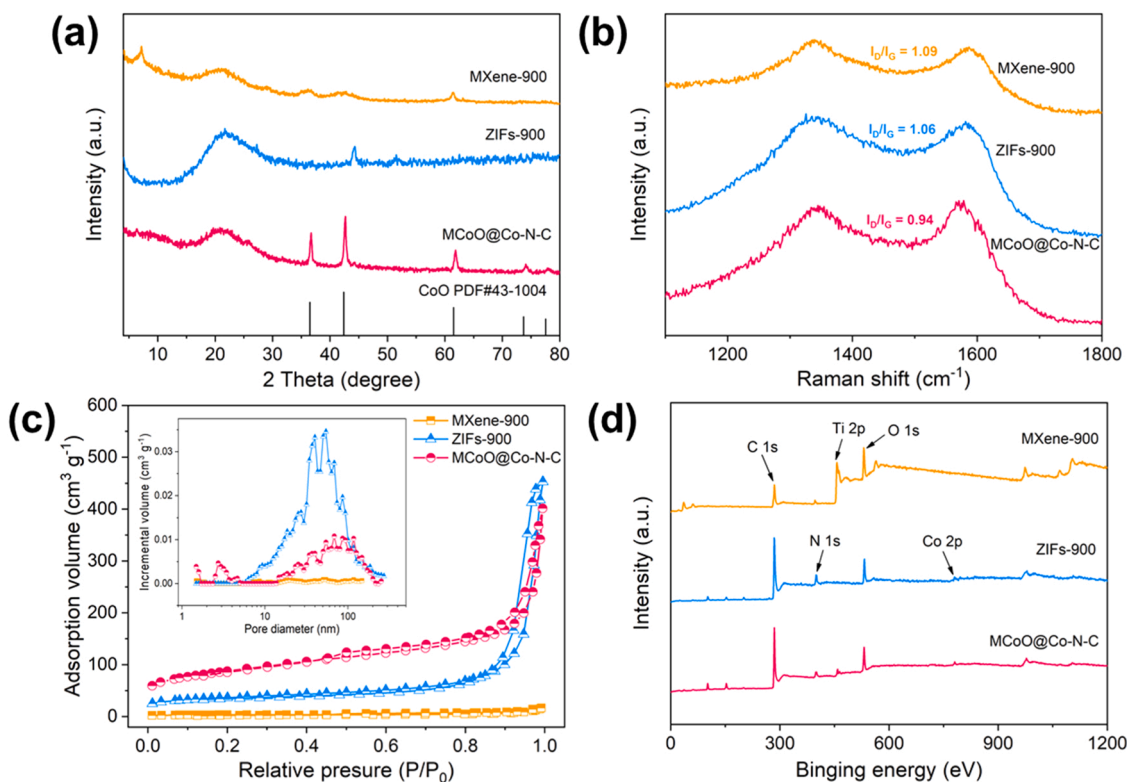

Fig. 2. (a) XRD pattern, (b) Raman spectra, (c) N_2 adsorption-desorption isotherm curves and the inset shows the pore size distribution, and (d) XPS survey spectra of MXene-900, ZIFs-900, and MCoO@Co-N-C.
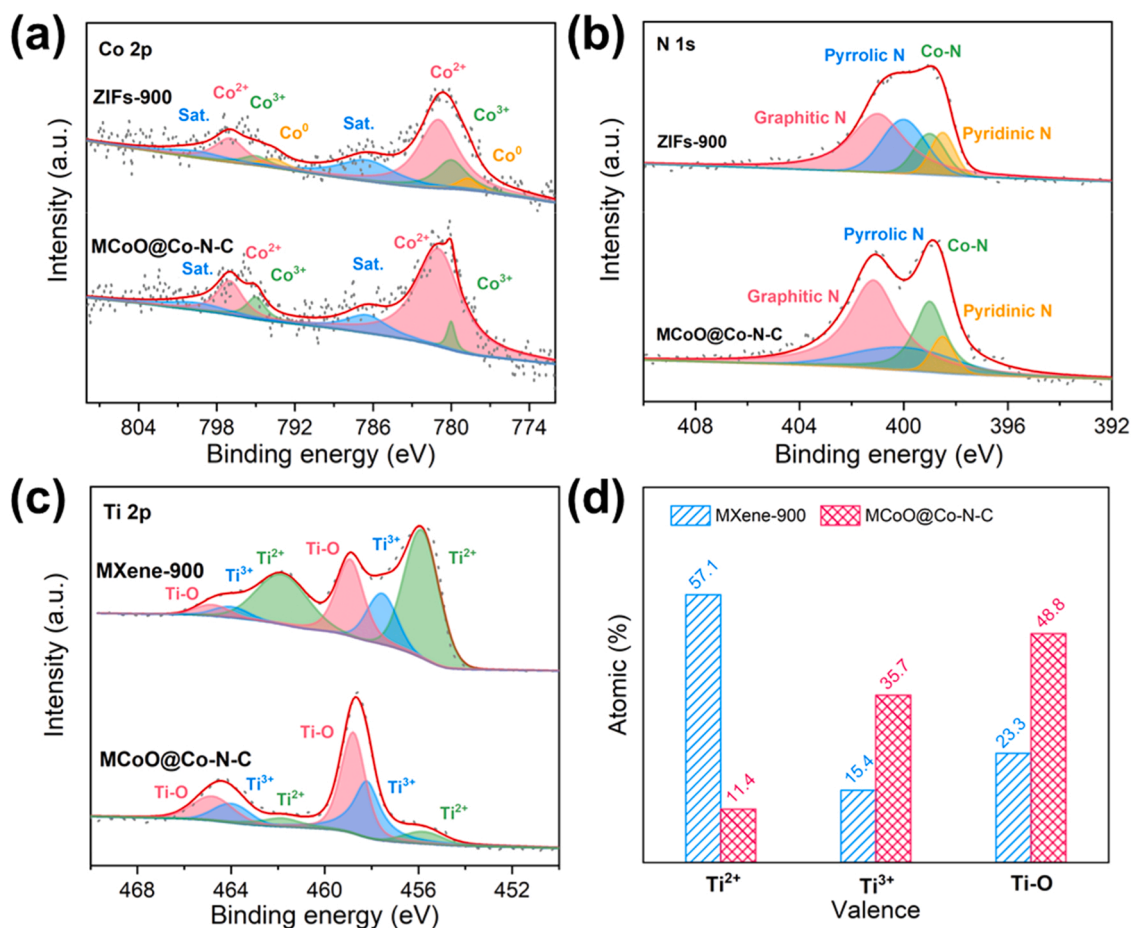
Fig. 3. XPS spectra of (a) Co, (b) N, and (c) Ti elements in MXene-900, ZIFs-900, and MCoO@Co-N-C samples; (d) percentages of diverse atomic Ti species (Ti^{2+}, Ti^{3+}, and Ti-O) of the MXene-900 and MCoO@Co-N-C.

of Co ions with $-O_x/-(OH)_x$ groups from MXene's terminal, further demonstrating the successful doping into MXene by cobalt, which provides evidence for rapid internal electron transport between MXene and CoO [40]. The chemical state of nitrogen was also evaluated by the high-resolution N 1 s XPS spectra. In the case of the MCoO@Co-N-C, the peaks at 398.5, 399, 400, and 401.1 eV correspond to pyridinic N, metal coordinated N (Co-N), pyrrolic N, and graphitic N, respectively (Fig. 3b) [6,41]. By comparison, the introduction of MXene was found to be more favorable for the formation of Co-N species. The Ti 2p XPS region of MCoO@Co-N-C (Fig. 3c) could be deconvoluted into six peaks belonging to Ti^{2+} (455.8/461.8 eV), Ti^{3+} (458.2/464.0 eV), and Ti-O (458.8/464.8 eV) respectively [42]. Particularly, the peaks assigned to Ti^{3+} and Ti-O from MCoO@Co-N-C began to get stronger compared with MXene-900, which increased from 15.4 at% (MXene-900) to 35.7 at% (MCoO@Co-N-C) for Ti^{3+}, and from 23.3 at% (MXene-900) to 48.8 at% (MCoO@Co-N-C) for Ti-O separately (Fig. 3d). Comparingly, the peaks originating from Ti^{2+} diminished considerably from 57.1 at% (MXene-900) to 11.4 at% (MCoO@Co-N-C), indicating the rise of Ti valence states in the hybrid. The change in Ti valence state suggests the coordination between MOFs and MXene during the carbonization process [43].

3.2. Performance of the MCoO@Co-N-C in PMS activation for BPA degradation

The catalytic performance of the prepared catalysts was evaluated by activating PMS for the degradation of BPA. As demonstrated in Fig. 4a, the degradation efficiency of BPA was negligible when PMS was present alone, indicating that PMS barely produces oxidizing radicals in the absence of catalysts. Meanwhile, BPA was hardly adsorbed by the catalyst, reducing about 12% of the BPA in 30 min. In contrast, when MCoO@Co-N-C and PMS were present simultaneously, the concentration of BPA started to decrease rapidly and more than 98% of BPA was decomposed in 10 min in which the pseudo-first-kinetics rate constants (k) reached 0.472 min^{-1} (Fig. 4b). The k value of MCoO@Co-N-C was higher than that of most previously reported catalysts for the degradation of BPA (Fig. 4c and Table S2) [44–55]. The inappreciable degradation efficiency (nearly 5%) was obtained in the MXene-900/PMS system, which meant that MXene-900 could not decompose BPA. In the ZIFs-900/PMS system (Fig. 4a), only about 25% of BPA was reduced within 30 min. The inferior performance might be attributed to the aggregation after pyrolysis caused by the small size of ZIFs NPs (about 60 nm) (Fig. S4c). The incorporation of MXene vigorously enhances the degradation efficiency, suggesting that the strong interaction between MXene and MOFs is more conducive to PMS activation and catalytic degradation of pollutants. To better comprehend the unique role of MXene, GO as a representative carbon material in place of MXene was used to fabricate ZIFs/GO-900. As demonstrated in Fig. S5, when MXene was replaced with GO, the degradation efficiency was considerably reduced, and the degradation of BPA was only around 10% in 30 min. This could be attributed to the increased overall conductivity of the catalyst as a result of the introduction of MXene, as well as the strong reduction of Ti atoms in MXene which promotes the Co(II)/Co(III) cycle and speeds up internal electron transfer [56]. Notably, even with tiny quantities of catalyst (0.05 g L^{-1}) and PMS (0.1 g L^{-1}), the as-prepared MCoO@Co-N-C catalyst displayed an extremely high TOF value (8.64 min^{-1}) (Table S2) due to its open sandwich-like heterostructure and high-density active sites. To further demonstrate the superiority of
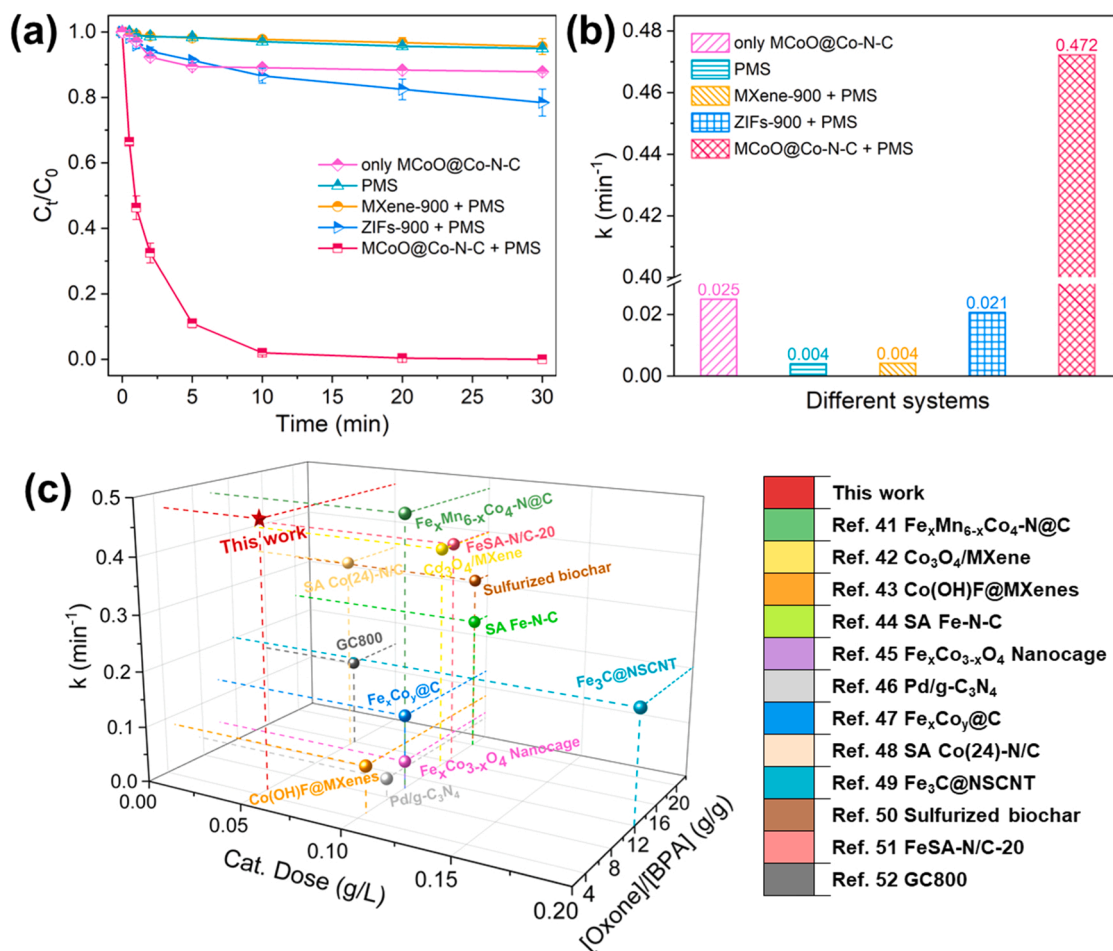
Fig. 4. (a) Degradation performance of BPA in different systems, [BPA] = 20 mg L^{-1}, [PMS] = 0.1 g L^{-1}, [catalysts] = 0.05 g L^{-1}, T = 25 ℃, initial pH = 3.7; (b) first-order kinetics curves of the corresponding catalysts; (c) comparisons of oxidative efficiency of MCoO@Co-N-C with those reported materials.

the sandwich-like derivative in which both sides of MXene nanosheets were almost completely covered by ZIFs, catalysts with different mass ratios of ZIFs/MXene were prepared. As displayed in Fig. S6, MCoO@Co-N-C exhibited the highest removal efficiency (100%) within 30 min compared to MCoO@Co-N-C-8 (87%) and MCoO@Co-N-C-4 (58%). For MCoO@Co-N-C-8, when MXene was loaded on excessive ZIFs, the extra ZIFs were unable to touch the surface of MXene and thus could not achieve the synergy effect. As for MCoO@Co-N-C-4, when the MXene surface was not fully covered by ZIFs, the active sites were correspondingly reduced. Therefore, only this unique sandwich-like structure is optimal for activating PMS to remove BPA.

Moreover, both temperature and pH are essential factors that influence catalytic performance. The higher oxidation efficiency of BPA was reached with the rise of the reaction solution temperature from Fig. S7a, which indicated that higher temperature was beneficial to improving the degradation efficiency of BPA. Considering the energy consumption, room temperature (25 ℃) was selected as the experimental condition temperature. As discussed in Fig. S7b, the final degradation rate of BPA appeared to be insensitive to the change in solution pH value. At pH = 3.7, MCoO@Co-N-C exhibited the highest activity. According to zeta potential (Fig. S8), the surface of the catalyst was more positively charged at pH = 3.7 to facilitate the adsorption of PMS, thus enhancing the interaction between PMS and catalyst [54].

3.3. Identification of ROS

Although various MXene-based composites have been known to have the ability to activate PMS for organic oxidation [57,58], the specific

mechanism is still unclear and needs to be further investigated. Therefore, scavenging experiments, as well as electron paramagnetic resonance (EPR) analysis, were applied to determine the ROS involved in the degradation of BPA in the MCoO@Co-N-C/PMS system. MeOH is usually employed as the scavenger for $SO_4^{\bullet-}$ ($k_{SO4\bullet-} = 3.2 \times 10^6$ M^{-1} s^{-1}) and $^{\bullet}OH$ ($k_{\bullet OH} = 9.7 \times 10^8$ M^{-1} s^{-1}), while TBA is chosen to detect $^{\bullet}OH$ ($k_{\bullet OH} = 9.7 \times 10^8$ M^{-1} s^{-1}) [59]. After adding excess scavengers (MeOH or TBA), completely no inhibition effect was observed for BPA removal (Fig. 5a), suggesting that the role of $SO_4^{\bullet-}$ and $^{\bullet}OH$ were negligible in this system. To further substantiate the point, EPR analysis was carried out with DMPO as the spin-trapping agent to identify $SO_4^{\bullet-}$/ $^{\bullet}OH$ and no obvious signal was found in the DMPO + MCoO@Co-N-C + PMS system (Fig. S9a). *p*-BQ was selected as the scavenger to identify $O_2^{\bullet-}$, the suppression effect was also trifling. The above results collectively speculate that the MCoO@Co-N-C/PMS system encounters a nonradical pathway.

Sulfoxides like DMSO are commonly used to detect the presence of high-valent metal species [60]. After the addition of 2 mM DMSO, the oxidative degradation of BPA showed no inhibition, indicating the insignificant function of high-valent metals species in the system. L-histidine was utilized to probe singlet oxygen ($^1O_2$), the addition of the quenching agent played a slightly suppressed effect during the degradation process. This result indicates that $^1O_2$ was not the predominant ROS in the system. In fact, the $^1O_2$ quencher of L-histidine could inevitably react with PMS, impeding the generation of other ROS. However, the quencher has a propensity for reacting with $^1O_2$ taking priority over PMS due to the reaction rate constant of L-histidine and $^1O_2$ ($k_{1O2, L-histidine} = 3.2 \times 10^7$ M^{-1} s^{-1}) is approximately 10^7 times higher than that with PMS ($k_{PMS, L-histidine} = 10.9$ M^{-1} s^{-1}) [61]. Hence, the data
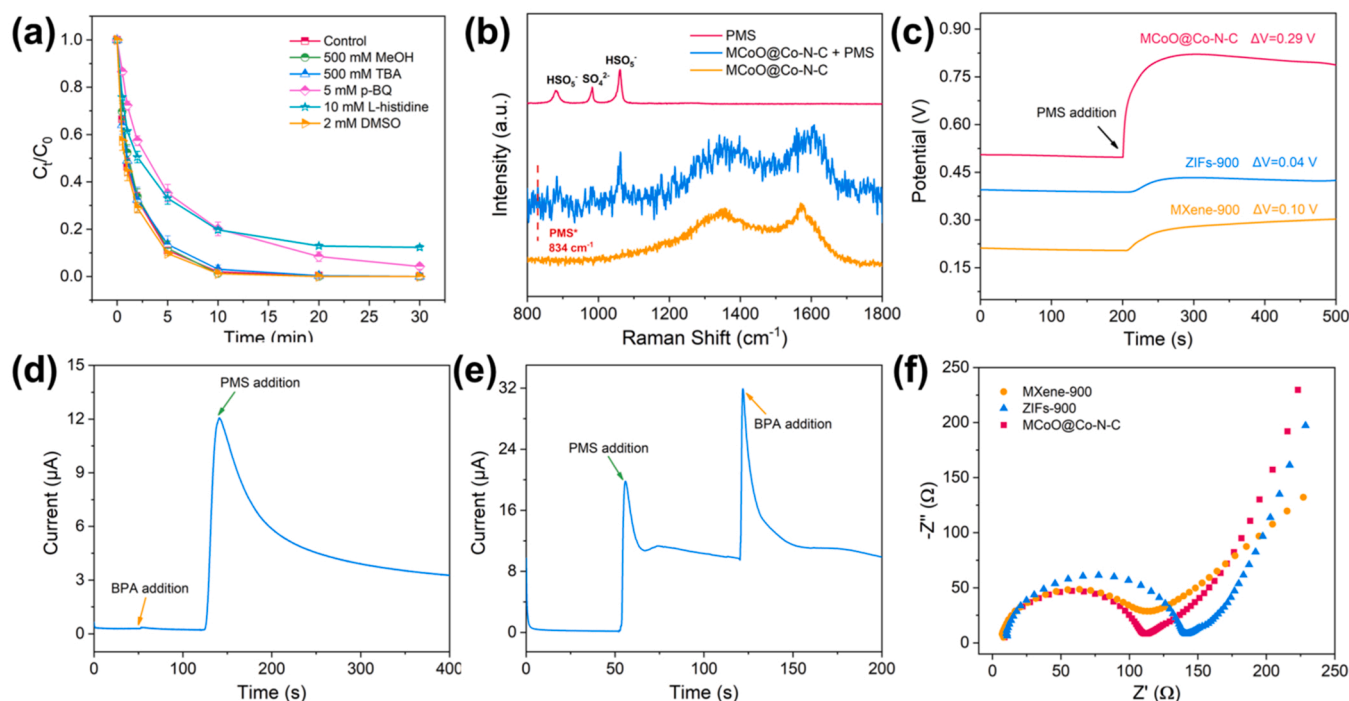
Fig. 5. Investigations of the electron transfer mechanism. (a) Effect of scavengers on BPA degradation in the MCoO@Co-N-C/PMS system, [BPA] = 20 mg L^{-1}, [PMS] = 0.1 g L^{-1}, [catalysts] = 0.05 g L^{-1}, T = 25 °C, initial pH = 3.7; (b) in situ Raman spectra of different samples; (c) variation of open circuit potential for different catalysts; (d, e) i-t curves obtained at 0 V vs. Ag/AgCl using 100 mM Na$_2$SO$_4$ as the electrolyte; (f) EIS Nyquist plots of the as-prepared catalysts.

from scavenging experiments is still credible. The EPR spectra were then performed to further unravel the mechanism in this system. TEMP as the typical spin trap was utilized to identify $^1O_2$. A distinctive three-line pattern originating from Fig. S9b appeared due to the probable decomposition of PMS [62]. After adding the catalyst, a slight change was detected in the EPR spectra, proving the minor function of $^1O_2$ in the nonradical process combined with the scavenging experiment.

Besides, K$_2$Cr$_2$O$_7$ was utilized as an electron scavenger to identify the ETP, which resulted in a significant decrease in BPA removal [62,63]. As shown in Fig. S10, the excessive concentration would accelerate the degradation of BPA due to the complicated side reactions. Therefore, it is of great importance to choose the appropriate doses. These results jointly show that ETP may play a dominant role in this system.

3.4. Electron-transfer pathway

Persulfate-based ETP typically consists of two steps: (i) reactant adsorption and persulfate activation; (ii) organics oxidation and SO$_4^{2-}$ generation. Generally, the reaction between catalyst and PMS consists of outer-sphere (electrostatic bonding) and inner-sphere (ionic or covalent bonding) interactions [11]. The reaction of PMS on the MCoO@Co-N-C surface can be indirectly evaluated by ionic interference experiments. The ionic strength can be adjusted by adding different amounts of perchlorate (0–120 mM NaClO$_4$) [7]. It has been reported that the thickness of the electric double layer on the surface of the particle will be compressed as ionic strength increases, essentially affecting the outer-sphere interaction between particles and solutes; however, increasing ionic strength has no effect on inner-sphere interactions [17]. As exhibited in Fig. S11, The degradation efficiency was hardly affected by the increasing ionic strength. This indicated the presence of inner-sphere interaction between PMS and the catalyst, suggesting the formation of MCoO@Co-N-C-PMS complex [63]. Besides, In situ X-ray absorption spectroscopy (XAS) can offer stronger direct evidence about the inner-sphere and outer-sphere interactions which could be utilized to validate the catalyst-PMS interaction of ETP in future studies [64,65]. Subsequently, In situ Raman spectra further demonstrated the formation

of the complex. In situ Raman spectra unveiled the transformation of the surface chemistry state between catalysts and PMS during the oxidation process. There was a new peak that appeared at 834 cm^{-1} after adding PMS in Fig. 5b, which was ascribed to the produced activated species (PMS*) [15,66].

Electrochemical analysis including open-circuit potentials, linear sweep voltammetry (LSV), chronoamperometry test, and electrochemical impedance spectra (EIS) tests were carried out to further corroborate electron transfer in the process of PMS activation. Tests of open-circuit potentials (Fig. 5c) uncovered the production of surface-active species on the catalyst during the nonradical process of activating PMS [15]. PMS addition triggered the increase of open-circuit potentials, which showed the formation of catalysts-PMS complexes along with the enhancement of oxidative capacity. Potentials changed larger for MCoO@Co-N-C-PMS (0.29 V) than for MXene-900-PMS (0.10 V) and ZIFs-900-PMS (0.04 V). The high potential of MCoO@Co-N-C-PMS (+ 0.8 V) was consistent with the large adsorption quantity of PMS (about 0.23 mM) (Fig. S12). This indicates that the superior activity of the catalyst allows for rapid mass transfer from the PMS to the MCoO@Co-N-C and generation of more MCoO@Co-N-C-PMS complex. LSV curves (Fig. S13) revealed the remarkable increase in current density after the injection of PMS. This scenario implied that MCoO@Co-N-C interacting with PMS formed a metastable reactive specie [67]. Besides, the addition of BPA resulted in another increase in current density, indicating electron transportation from BPA to PMS was highly dependent on the interrelationship between BPA and PMS on the catalytic surface [68]. Meanwhile, chronoamperometry tests were also conducted to analyze the intrinsic kinetics of electron transfer. As demonstrated in Fig. 5d, after dosing BPA initially, no significant variations of current density occurred between the catalyst and BPA. However, when PMS was added in advance (Fig. 5e), a significant positive current flow appeared rapidly, suggesting the generation of surface-active complexes between PMS and the catalyst. The subsequent injection of BPA gave rise to a drastic positive current peak, indicating electron migration from BPA to the catalyst surface. In order to further investigate the number of electrons transferred reflected by current, a

combined technique of open circuit potential and chronoamperometry was performed [69]. As shown in Fig. S14a, following the addition of PMS, the open circuit potential elevated rapidly and formed a MCoO@Co-N-C-PMS complex, eventually stabilizing at about + 0.8 V. Combine with chronoamperometry (Fig. S14b), no significant difference in current with or without the presence of BPA when the applied potential (+ 0.45 V) was less than the oxidation potential of BPA (about 0.5 V at pH=7.3). However, while the applied potential reached the equilibrium potential of MCoO@Co-N-C-PMS complex (+ 0.8 V) and exceeded the oxidation potential of BPA, the current in the presence of BPA was substantially higher than in the absence of BPA. This suggests that electron donor can expedite ETP as the potential of MCoO@Co-N-C-PMS complex surpasses the oxidation potential of BPA. These data collectively show that MCoO@Co-N-C was performed as an "electronic bridge" to promote electron transfer from BPA to PMS for achieving degradation of contaminants. To validate the theory, the electrochemical characteristics of the catalysts were studied by EIS. Fig. 5f demonstrated that MCoO@Co-N-C had a smaller semicircular diameter and a faster rate of mass transfer compared to MXene-900 and ZIFs-900 systems. This denoted a superior conductivity of MCoO@Co-N-C thus favorably facilitating electron transfer [70]. Tafel slope is an important parameter for evaluating catalysts in electrochemistry. The Tafel slope value of MCoO@Co-N-C was calculated by fitting the Tafel curve to the Tafel equation (Fig. S15 and Text S1), which is 130 mV dec^{-1}, indicating the excellent electrochemical performance

[15,71]. The above results provide strong evidence for electron migrating from BPA to PMS in the presence of the catalyst.

3.5. Theoretical calculations

DFT calculations further reveal the mechanism role of the catalyst in ETP. The highest occupied molecular orbital (HOMO) and lowest unoccupied molecular orbital (LUMO) gap are employed to probe the process of potential energy difference-driven electron transfer. The gap between HOMO and LUMO of MCoO@Co-N-C (0.3931 eV) greatly decreases compared to Co-N-C (0.9287 eV) in Fig. S16. Due to the lower energy barrier of MCoO@Co-N-C, the catalyst is more prone to electron transfer. Integrated with the above results, molecular orbital (MO) energy graphs dominated by the electron transfer mechanism are proposed. Fig. 6a demonstrates that electrons are first transported from HOMO (-5.845 eV) of BPA to LUMO (-4.305 eV) of MCoO@Co-N-C. As a result of the narrowest energy gap (0.3931 eV) of MCoO@Co-N-C, electron transport from LUMO to HOMO is easier. The catalyst then acts as a conductive bridge to transfer electrons to PMS, inducing the decomposition of PMS. Moreover, as evidenced by the charge density difference of PMS adsorbed on MCoO@Co-N-C (Fig. 6b), the electron depletion region is located around the Co center, whereas the electron accumulation region occurs on the O atoms of PMS. The significant electron transfer between PMS and MCoO@Co-N-C reflects the chemisorption of PMS on the substrate, which is consistent with the stronger
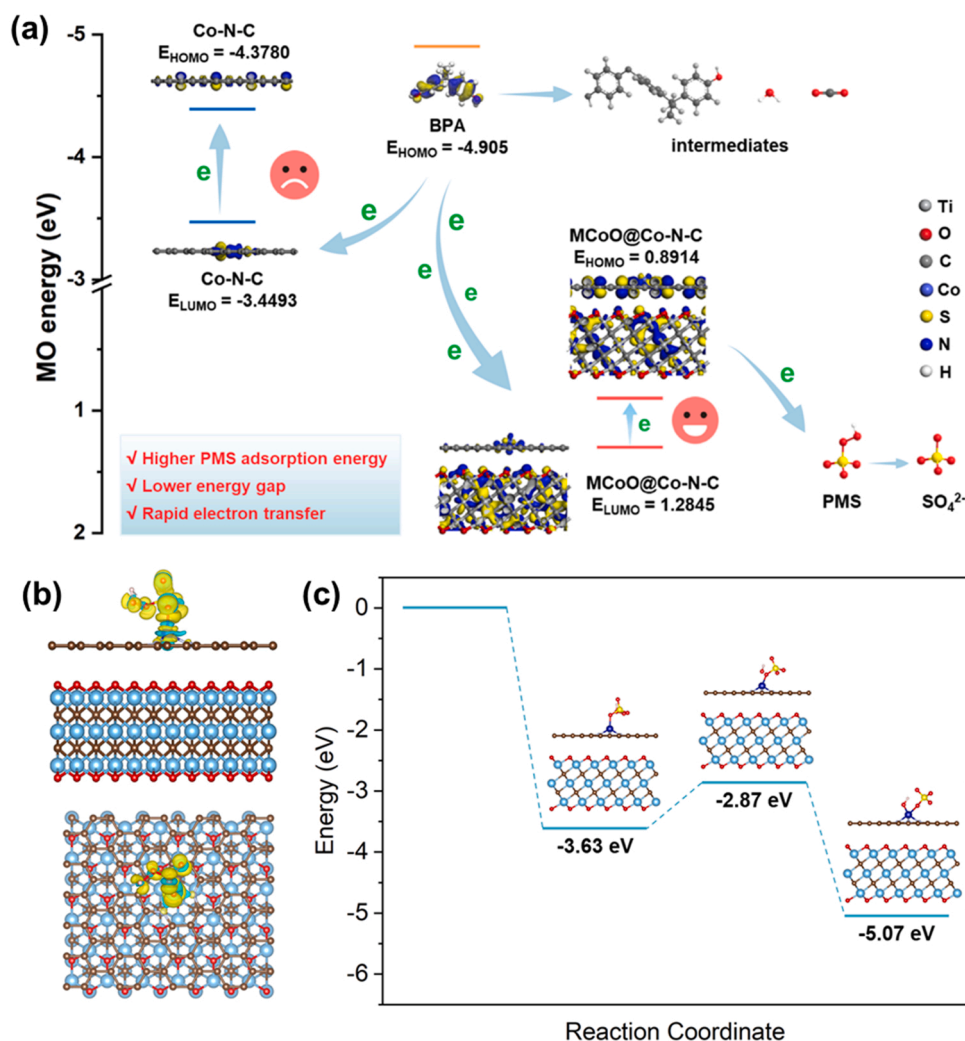

Fig. 6. (a) ETP for BPA oxidation induced by potential energy difference; (b) charge density difference of the adsorption of PMS on MCoO@Co-N-C, where blue and yellow represent electron depletion and electron accumulation, respectively; (c) energy profile during the dissociation of PMS.

PMS adsorption energy (E_{ads}) of MCoO@Co-N-C (−3.63 eV) (Fig. S17). This indicates that Co-N species become more adsorptive to PMS after the hybridization of MXene and MOF. The possible energy profile during the dissociation of PMS is also calculated to understand the possible reaction pathways (Fig. 6c). The whole process of PMS decomposition over the catalyst is found to be spontaneous with the reaction barrier of 0.76 eV by simulating the reaction kinetics. According to calculations on the adsorption and decomposition of PMS, PMS prefers to adsorb on the Co-N site. Afterward, the OH* moiety is released and attaches to Co-N site, and then the final state complex would obtain electrons to generate SO_4^{2-} and OH^-. This is in agreement with the previously postulated ETP. These results collectively provide solid support for an electron transfer-dominated mechanism.

3.6. Activation mechanism of MCoO@Co-N-C

To better understand the involved mechanism, different characterizations of used catalysts including XRD, Raman, and XPS are conducted. In the XRD patterns (Fig. S18a), the diffraction peak at 25.3° indexed as the (101) plane of TiO_2 got stronger, indicating a valence change in Ti species. The presence of TiO_2 was further confirmed by Raman spectra of the catalyst before and after the reaction (Fig. S18b). The two strong peaks at 154 and 206 cm^{-1} belong to anatase phase TiO_2 [72]. Meanwhile, the structural changes on the catalyst surface were also explored by Raman spectroscopy (Fig. S18c). The intensity ratio of I_D/I_G decreased from 0.94 to 0.81, indicating a reduction in surface defects and an increase in graphitization. This could be because the structural flaws and dangling bonds produced by the pyrolysis of oxygen-containing groups would encourage the recombination of these unsaturated carbon atoms into graphitic phases [73]. Additionally, metals (Ti, Co) might function as catalysts to greatly speed up the rate of surface graphitization [74]. The enhancement of graphitization results in the increase of conductivity, which will facilitate the activation of PMS through the electron transfer pathway [75]. From the XPS analysis before and after reactions, no obvious changes in the valence states of Ti, Co, and N elements were discerned (Fig. S19a-c). However, their atomic content was greatly decreased (Table S3), probably because these elements were involved in the reaction and the active sites were masked by the produced intermediates. To prove the point, ICP-OES was used to explore the content of Co element in the fresh and used catalyst and the leaching of Co after reactions. The mass fraction of Co was kept almost unchanged before and after reactions (Table S4). In addition, the degradation efficiency of BPA (9%) by the amount of Co leaked (0.026 mg L^{-1}) was nearly negligible (Fig. S20a and b). These results provide strong evidence that the catalyst was covered by the generated intermediates. Based on the above analysis, a possible catalytic mechanism for the oxidative degradation of BPA by activating PMS with an electron-transfer pathway in the MCoO@Co-N-C system is deduced as follows (Fig. 7): BPA is initially adsorbed on the catalyst surface, followed by PMS adsorption via the Co-N species of the catalyst [51]. The interaction between PMS and Co-N species produces surface-bound active complexes through the inner-sphere interaction. Subsequently, the high electrical conductivity of MXene and CoO enables rapid interfacial charge transfer to the carbon atoms on the catalyst surface, which affects the active sites and charge distribution on the carbon shell [76]. The rapid electron transfer between MXene and CoO was achieved by the oxidation of Co(II)/Ti(II) and the reduction of Co(III)/Ti(IV). When Co(II) was oxidized to Co(III) in the activation of PMS, the strong reductivity of Ti(II)/Ti(III) in $Ti_3C_2T_x$ made Co(III) reduce to Co(II) [39, 57]. As a result, Ti(II)/Ti(III) was oxidized to Ti(IV), which was consistent with the variation of peak intensity of TiO_2 in XRD and Raman as well as relative peak areas (from 48% to 52% after reaction) of Ti-O bond in XPS. The existence of MXene achieved Co(II)/Co(III) cycle and accelerated interfacial electron transfer from MXene to CoO. These potential active sites markedly enhance the decomposition of pollutants via mediating the transfer of electrons from the BPA to PMS.
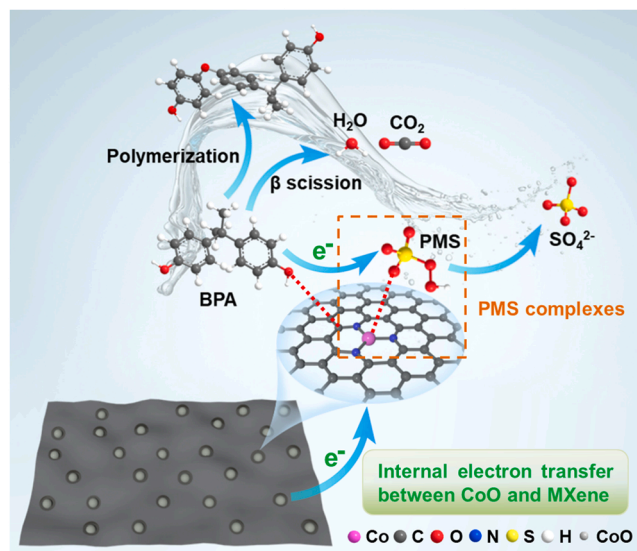

Fig. 7. Proposed electron-transfer mechanism for PMS activation by MCoO@Co-N-C.

3.7. The degradation of BPA under high salinity conditions

Inorganic anions are ubiquitously found in practical wastewater. According to previous literature [62,70], as is known that anions pose a great influence on radicals ($SO_4^{\bullet-}$ and $^{\bullet}OH$) while exhibiting an insubstantial impact on nonradical-based AOPs. To investigate the effect of high anion concentrations on the MCoO@Co-N-C/PMS system, we selected four representative anions of different concentrations including Cl^-, NO_3^-, HCO_3^-, and $H_2PO_4^-$. With the analogical orderliness, even when the anion concentration was 200 mM, the effects of Cl^-, $H_2PO_4^-$, NO_3^-, and HCO_3^- on the MCoO@Co-N-C/PMS system could also be ignored (Fig. 8a-d). However, the co-existing NO_3^- had a slightly negative influence on the degradation of BPA. The minor inhibition of NO_3^- (Fig. 8b) might be attributed to the competition between nitrate and pollutants [9]. Besides, the presence of HCO_3^- (Fig. 8d) resulted in a slight promotion of PMS activation, whose function as buffering reagents might be strengthened the ability of electron transfer by adjusting the pH value [54]. In general, no significant inhibition effects are observed on the degradation rate of BPA in the existence of anions, which further demonstrates the strong anti-interference ability in complicated water matrices of nonradical-based AOPs.

Furthermore, due to the electron-transfer oxidation regime, ETP is usually selective for target organics. The properties of organic substrates have a large impact on the selectivity of ETP systems. Bisphenol A (BPA), Phenol (PE), p-nitrophenol (p-NP), and benzoic acid (BA) were selected as target contaminants based on their different ionization potential (IP) which reflect the ability of electron-donating/electron-withdrawing [12]. As presented in Fig. S21, the MCoO@Co-N-C/PMS system showed excellent selectivity with 5%, 55%, 83%, and 100% degradation of BA, p-NP, PE, and BPA, respectively. This can effectively avoid competing reactions for the coexistence of components in complex environments, providing a promising platform for practical wastewater treatment.

3.8. Degradation pathway of BPA and removal of TOC

To gain further insight into the degradation pathway of BPA, the intermediates produced during the decomposition process as well as the extraction of products adsorbed onto the catalytic surface are separately detected by LC-MS/MS (Table S5). A total of nine transformation products were detected and two major degradation pathways were proposed as presented in Fig. 9. In pathway I, BPA (TP1) was expected to
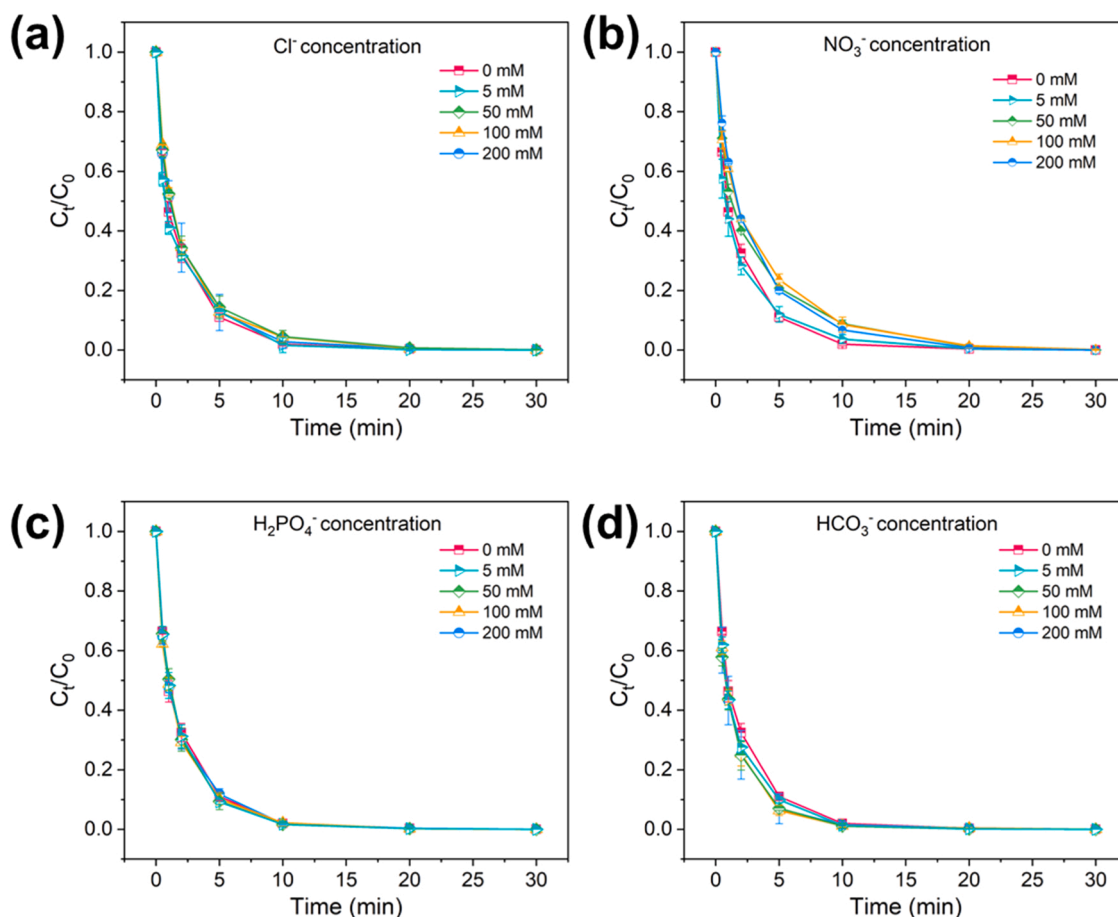
Fig. 8. Effects of organic anions (a) Cl^-, (b) NO_3^-, (c) $H_2PO_4^-$, and (d) HCO_3^-, [BPA] = 20 mg L^{-1}, [PMS] = 0.1 g L^{-1}, [catalysts] = 0.05 g L^{-1}, T = 25 °C, initial pH = 3.7.
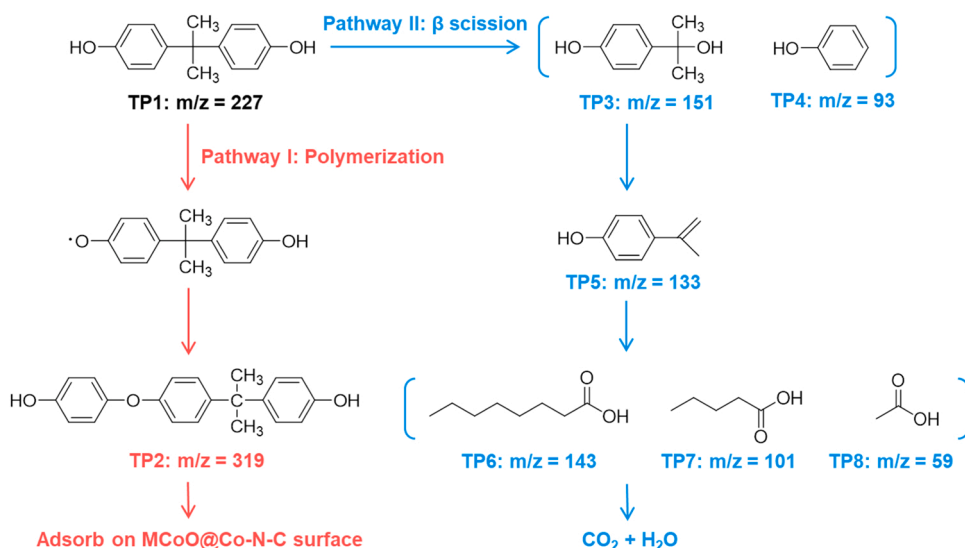

Fig. 9. Possible degradation pathways of BPA in MCoO@Co-N-C/PMS systems.

lose an electron after being oxidized, generating a phenoxy radical [77]. It was further polymerized to 4-(2-(4-(4-hydroxyphenoxy)phenyl) propan-2-yl)phenol (TP2) via coupling elimination, which was probably adsorbed on the catalyst. Moreover, The ROS based on electron-transfer pathway tends to attack electron-rich pollutants, which are usually broken from the strong nucleophilic sites [53]. In pathway-II, β-scission

of isopropyl in two phenyl occurred to produce 4-(2-hydroxy-2-propyl) phenol (TP3) and phenol (TP4), then TP3 further transformed as 4-iso-propenylphenol (TP5). Subsequently, these intermediates underwent ring cleavage to generate various organic acids including octanoic acid (TP6), pentanoic acid (TP7), and acetic acid (TP8), which were eventually mineralized to carbon dioxide (CO_2) and water (H_2O). Even

though these oligomeric intermediates may cause potentially toxic concerns, they are primarily adsorbed on the catalyst surface and almost insoluble in the aqueous phase [78]. Concomitantly, these active sites are blocked by these intermediates, leading to the deactivation of the catalyst. Only 22% of the BPA in the third cycle was decomposed within 30 min (Fig. S22). Facile post-treatment methods including thermal treatment and extracting by MeOH [79] were applied to regenerate the catalyst. The catalytic activity of spent MCoO@Co-N-C could be reactivated via these post-treatment methods. Compared with MeOH extraction (67%), the degradation efficiency of thermal treatment (97%) after the third run was more remarkable. Furthermore, the addition of natural organic matters (NOM) such as humic acid (HA) in concentrations ranging from 0 to 20 mM had little effect on the BPA removal efficiency (Fig. S23). The performance of the catalyst was also evaluated for the degradation of BPA spiked in different water matrixes including deionized water, tap water, and river water (Fig. S24a). The removal efficiency of BPA (100% within 30 min) in different matrixes was hardly affected by the interference of numerous anions and natural organic matters (NOM), indicating the huge potential for practical wastewater treatment. Besides, the mineralization ability of the catalyst was evaluated by measuring TOC in different water quality (Fig. S24b). MCoO@Co-N-C exhibited a high TOC removal in deionized water (70.8%) and tap water (68.5%) but only 26.5% in river water, which might be due to excessive NOM adsorption. The high removal of TOC might be attributed to two reasons: (i) the mineralization of BPA into CO_2 and H_2O via β-scission as displayed in pathway II; (ii) the enrichment of the intermediate polymer converted from BPA on the catalyst surface for rapid carbon migration, thus effectively removing contaminants from the water.

Additionally, the acute and chronic toxicity of BPA and its degradation intermediates was predicted using ECOSAR program (version 2.0) (Fig. S25). The acute toxicity is divided into four categories by the European Union criteria: extremely toxic (< 1 mg L^{-1}), toxic (1–10 mg L^{-1}), harmful (10–100 mg L^{-1}) and harmless (> 100 mg L^{-1}). While the Chinese hazard chemical evaluation guidelines (HJ/TI 154–2004) were used to classify chronic toxic levels: extremely toxic (< 0.1 mg L^{-1}), toxic (0.1–1 mg L^{-1}), harmful (1–10 mg L^{-1}), and harmless (> 10 mg L^{-1}). Three aquatic organisms including fish, daphnid and green algae exhibited acute toxicity toward BPA. In terms of chronic toxicity, it is harmful to daphnid, but toxic for fish and green algae. The majority of the $LC_{50}/EC_{50}/ChV$ values for the degradation intermediates showed a rising trend, indicating a decrease in biotoxicity. Between them, TP6, TP7, and TP8 are even harmless. The polymerization product TP2 of BPA was extremely toxic, but the intermediate would be enriched on the surface of the catalyst, thus enabling further removal. In general, the biological toxicity of BPA will be greatly reduced after degradation by the MCoO@Co-N-C/PMS system.

4. Conclusion

In summary, the electron-transfer mechanism is proposed in the MCoO@Co-N-C/PMS system and the effect of different inorganic anions on the degradation of BPA under high concentrations is investigated simultaneously. The 2D MXene material with superior electrical conductivity has been shown to facilitate electron transfer in the monolithic catalyst. The uniquely open sandwich-like structure not only enhances the adsorption of PMS via the Co-N species but efficiently enables the rapid internal electron transfer between MXene and CoO. The rational design of catalysts provides new insight into the activation of PMS to degrade refractory pollutants via an intriguing nonradical pathway. This work provides a viable framework for the application of MXene-based composites in AOPs to remove contaminants in a complicated water matrix.

CRediT authorship contribution statement

Xin Guo: Conceptualization, Methodology, Writing – original draft. **Hao Zhang:** Conceptualization, Methodology. **Yiyuan Yao:** Methodology, Formal analysis. **Chengming Xiao:** Software, Data curation. **Xin Yan:** Software, Validation. **Ke Chen:** Formal analysis, Data curation. **Junwen Qi:** Investigation, Supervision. **Yujun Zhou:** Resources. **Zhigao Zhu:** Visualization. **Xiuyun Sun,** Investigation, Visualization. **Jiansheng Li:** Conceptualization, Writing – review & editing, Supervision, Project administration; Funding acquisition.

Declaration of Competing Interest

The authors declare that they have no known competing financial interests or personal relationships that could have appeared to influence the work reported in this paper.

Data Availability

Data will be made available on request.

Acknowledgements

Appendix A. Supporting information

Supplementary data associated with this article can be found in the online version at doi:10.1016/j.apcatb.2022.122136.

References

[1] P.J.J. Alvarez, C.K. Chan, M. Elimelech, N.J. Halas, D. Villagrán, Emerging opportunities for nanotechnology to enhance water security, Nat. Nanotechnol. 13 (2018) 634–641.

[2] J. Lee, U. von Gunten, J.H. Kim, Persulfate-based advanced oxidation: critical assessment of opportunities and roadblocks, Environ. Sci. Technol. 54 (2020) 3064–3081.

[3] Y. Peng, G. Xie, P. Shao, W. Ren, M. Li, Y. Hu, L. Yang, H. Shi, X. Luo, A comparison of SMX degradation by persulfate activated with different nanocarbons: kinetics, transformation pathways, and toxicity, Appl. Catal. B: Environ. 310 (2022), 121345.

[4] W. Tian, H. Zhang, Z. Qian, T. Ouyang, H. Sun, J. Qin, M.O. Tadé, S. Wang, Bread-making synthesis of hierarchically Co@C nanoarchitecture in heteroatom doped porous carbons for oxidative degradation of emerging contaminants, Appl. Catal. B Environ. 225 (2018) 76–83.

[5] Y. Wang, X. Zhao, D. Cao, Y. Wang, Y. Zhu, Peroxymonosulfate enhanced visible light photocatalytic degradation bisphenol A by single-atom dispersed Ag mesoporous g-C$_3$N$_4$ hybrid, Appl. Catal. B Environ. 211 (2017) 79–88.

[6] Y. Yao, C. Wang, X. Yan, H. Zhang, C. Xiao, J. Qi, Z. Zhu, Y. Zhou, X. Sun, X. Duan, J. Li, Rational regulation of Co-N-C coordination for high-efficiency generation of $^1O_2$ toward nearly 100% selective degradation of organic pollutants, Environ. Sci. Technol. 56 (2022) 8833–8843.

[7] Y. Yang, P. Zhang, K. Hu, P. Zhou, Y. Wang, A.H. Asif, X. Duan, H. Sun, S. Wang, Crystallinity and valence states of manganese oxides in Fenton-like polymerization of phenolic pollutants for carbon recycling against degradation, Appl. Catal. B: Environ. 315 (2022), 121593.

[8] W. Ren, L. Xiong, G. Nie, H. Zhang, X. Duan, S. Wang, Insights into the electron-transfer regime of peroxydisulfate activation on carbon nanotubes: the role of oxygen functional groups, Environ. Sci. Technol. 54 (2020) 1267–1275.

[9] X. Cheng, H. Guo, Y. Zhang, G.V. Korshin, B. Yang, Insights into the mechanism of nonradical reactions of persulfate activated by carbon nanotubes: activation performance and structure-function relationship, Water Res. 157 (2019) 406–414.

[10] H. Li, J. Shang, Z. Yang, W. Shen, Z. Ai, L. Zhang, Oxygen vacancy associated surface Fenton chemistry: surface structure dependent hydroxyl radicals generation and substrate dependent reactivity, Environ. Sci. Technol. 51 (2017) 5685–5694.

[11] W. Ren, C. Cheng, P. Shao, X. Luo, H. Zhang, S. Wang, X. Duan, Origins of electron-transfer regime in persulfate-based nonradical oxidation processes, Environ. Sci. Technol. 56 (2022) 78–97.

[12] P. Hu, H. Su, Z. Chen, C. Yu, Q. Li, B. Zhou, P.J.J. Alvarez, M. Long, Selective degradation of organic pollutants using an efficient metal-free catalyst derived

from carbonized polypyrrole via peroxymonosulfate activation, Environ. Sci. Technol. 51 (2017) 11288–11296.

[13] P. Duan, J. Pan, W. Du, Q. Yue, B. Gao, X. Xu, Activation of peroxymonosulfate via mediated electron transfer mechanism on single-atom Fe catalyst for effective organic pollutants removal, Appl. Catal. B: Environ. 299 (2021), 120714.

[14] S.H. Ho, Y. Chen, R. Li, C. Zhang, Y. Ge, G. Cao, M. Ma, X. Duan, S. Wang, N. Ren, N-doped graphitic biochars from C-phycocyanin extracted Spirulina residue for catalytic persulfate activation toward nonradical disinfection and organic oxidation, Water Res. 159 (2019) 77–86.

[15] W. Ren, G. Nie, P. Zhou, H. Zhang, X. Duan, S. Wang, The Intrinsic nature of persulfate activation and N-doping in carbocatalysis, Environ. Sci. Technol. 54 (2020) 6438–6447.

[16] H. Lee, H.I. Kim, S. Weon, W. Choi, Y.S. Hwang, J. Seo, C. Lee, J.H. Kim, Activation of persulfates by graphitized nanodiamonds for removal of organic compounds, Environ. Sci. Technol. 50 (2016) 10134–10142.

[17] T. Zhang, Y. Chen, Y. Wang, J. Le Roux, Y. Yang, J.P. Croué, Efficient peroxydisulfate activation process not relying on sulfate radical generation for water pollutant degradation, Environ. Sci. Technol. 48 (2014) 5868–5875.

[18] L. Wang, J. Jiang, S.Y. Pang, Y. Zhou, J. Li, S. Sun, Y. Gao, C. Jiang, Oxidation of bisphenol A by nonradical activation of peroxymonosulfate in the presence of amorphous manganese dioxide, Chem. Eng. J. 352 (2018) 1004–1013.

[19] M. Zhang, C. Xiao, X. Yan, S. Chen, C. Wang, R. Luo, J. Qi, X. Sun, L. Wang, J. Li, Efficient removal of organic pollutants by metal-organic framework derived Co/C yolk-shell nanoreactors: size-exclusion and confinement effect, Environ. Sci. Technol. 54 (2020) 10289–10300.

[20] C. Xiao, M. Zhang, C. Wang, X. Yan, H. Zhang, S. Chen, Y. Yao, J. Qi, S. Zhang, J. Li, 2D metal-organic framework derived hollow Co/NC carbon sheets for peroxymonosulfate activation, Chem. Eng. J. 444 (2022), 136385.

[21] C. Wang, J. Kim, J. Tang, M. Kim, H. Lim, V. Malgras, J. You, Q. Xu, J. Li, Y. Yamauchi, New strategies for novel MOF-derived carbon materials based on nanoarchitectures, Chem 6 (2020) 19–40.

[22] M. Zhao, X. Xie, C.E. Ren, T. Makaryan, B. Anasori, G. Wang, Y. Gogotsi, Hollow MXene spheres and 3D macroporous MXene frameworks for Na-ion storage, Adv. Mater. 29 (2017), 1702410.

[23] S.J. Kim, H.J. Koh, C.E. Ren, O. Kwon, K. Maleski, S.Y. Cho, B. Anasori, C.K. Kim, Y. K. Choi, J. Kim, Y. Gogotsi, H.T. Jung, Metallic $Ti_3C_2T_x$ MXene gas sensors with ultrahigh signal-to-noise ratio, ACS Nano 12 (2018) 986–993.

[24] Á. Morales-García, F. Calle-Vallejo, F. Illas, MXenes: New horizons in catalysis, ACS Catal. 10 (2020) 13487–13503.

[25] L. Zhao, B. Dong, S. Li, L. Zhou, L. Lai, Z. Wang, S. Zhao, M. Han, K. Gao, M. Lu, X. Xie, B. Chen, Z. Liu, X. Wang, H. Zhang, H. Li, J. Liu, H. Zhang, X. Huang, W. Huang, Interdiffusion reaction-assisted hybridization of two-dimensional metal-organic frameworks and $Ti_3C_2T_x$ nanosheets for electrocatalytic oxygen evolution, ACS Nano 11 (2017) 5800–5807.

[26] L. Yao, Q. Gu, X. Yu, Three-dimensional MOFs@MXene aerogel composite derived MXene threaded hollow carbon confined CoS nanoparticles toward advanced alkali-ion batteries, ACS Nano 15 (2021) 3228–3240.

[27] Z. Ye, Y. Jiang, L. Li, F. Wu, R. Chen, Self-assembly of 0D–2D heterostructure electrocatalyst from MOF and MXene for boosted lithium polysulfide conversion reaction, Adv. Mater. 33 (2021), 2101204.

[28] X. Shen, Y. Xiong, R. Hai, F. Yu, J. Ma, All-MXene-based integrated membrane electrode constructed using $Ti_3C_2T_x$ as an intercalating agent for high-performance desalination, Environ. Sci. Technol. 54 (2020) 4554–4563.

[29] L. Jiang, J. Duan, J. Zhu, S. Chen, M. Antonietti, Iron-cluster-directed synthesis of 2D/2D Fe-N-C/MXene superlattice-like heterostructure with enhanced oxygen reduction electrocatalysis, ACS Nano 14 (2020) 2436–2444.

[30] Y. Tian, X. Liu, L. Xu, D. Yuan, Y. Dou, J. Qiu, H. Li, J. Ma, Y. Wang, D. Su, S. Zhang, Engineering crystallinity and oxygen vacancies of Co(II) Oxide nanosheets for high performance and robust rechargeable Zn-air batteries, Adv. Funct. Mater. 31 (2021), 2101239.

[31] M. Wu, G. Zhang, H. Tong, X. Liu, L. Du, N. Chen, J. Wang, T. Sun, T. Regier, S. Sun, Cobalt (II) oxide nanosheets with rich oxygen vacancies as highly efficient bifunctional catalysts for ultra-stable rechargeable Zn-air flow battery, Nano Energy 79 (2021), 105409.

[32] X. Wang, S. Kajiyama, H. Iinuma, E. Hosono, S. Oro, I. Moriguchi, M. Okubo, A. Yamada, Pseudocapacitance of MXene nanosheets for high-power sodium-ion hybrid capacitors, Nat. Commun. 6 (2015) 6544.

[33] M. Ding, W. Chen, H. Xu, C. Lu, T. Lin, Z. Shen, H. Tao, K. Zhang, Synergistic features of superoxide molecule anchoring and charge transfer on two-dimensional $Ti_3C_2T_x$ MXene for efficient peroxymonosulfate activation, ACS Appl. Mater. Interfaces 12 (2020) 9209–9218.

[34] H. Zhong, J. Wang, Y. Zhang, W. Xu, W. Xing, D. Xu, Y. Zhang, X. Zhang, ZIF-8 derived graphene-based nitrogen-doped porous carbon sheets as highly efficient and durable oxygen reduction electrocatalysts, Angew. Chem. Int. Ed. 53 (2014) 14235–14239.

[35] R. Gao, Z. Li, X. Zhang, J. Zhang, Z. Hu, X. Liu, Carbon-dotted defective CoO with oxygen vacancies: a synergetic design of bifunctional cathode catalyst for Li-O_2 batteries, ACS Catal. 6 (2016) 400–406.

[36] M. Zhang, J. Ruan, L. Wang, Z. Zhao, W. Shao, J. Li, Z. Chen, C. Gu, W. Qiao, MXene-like carbon sheet/carbon nanotubes derived from metal-organic frameworks for efficient removal of tetracycline by non-radical dominated advanced oxidation processes, Sep. Purif. Technol. 300 (2022), 121851.

[37] C. Liu, J. Wang, J. Li, M. Zeng, R. Luo, J. Shen, X. Sun, W. Han, L. Wang, Synthesis of N-doped hollow-structured mesoporous carbon nanospheres for high-performance supercapacitors, ACS Appl. Mater. Interfaces 8 (2016) 7194–7204.

[38] X. Liang, X. Ren, Q. Yang, L. Gao, M. Gao, Y. Yang, H. Zhu, G. Li, T. Ma, A. Liu, A two-dimensional MXene-supported metal-organic framework for highly selective ambient electrocatalytic nitrogen reduction, Nanoscale 13 (2021) 2843–2848.

[39] D. Zu, H. Song, C. Li, Y. Wang, R. Du, R. Zhou, W. Zhang, S. Pan, Y. Cai, Y. Shen, Z. Yang, Understanding the self-catalyzed decomplexation mechanism of Cu-EDTA in $Ti_3C_2T_x$ MXene/peroxymonosulfate process, Appl. Catal. B: Environ. 306 (2022), 121131.

[40] Y. Deng, T. Shang, Z. Wu, Y. Tao, C. Luo, J. Liang, D. Han, R. Lyu, C. Qi, W. Lv, F. Kang, Q. Yang, Fast gelation of $Ti_3C_2T_x$ MXene initiated by metal ions, Adv. Mater. 31 (2019), 1902432.

[41] M. Li, S. Chen, Q. Jiang, Q. Chen, X. Wang, Y. Yan, J. Liu, C. Lv, W. Ding, X. Guo, Origin of the activity of Co-N-C catalysts for chemoselective hydrogenation of nitroarenes, ACS Catal. 11 (2021) 3026–3039.

[42] L. Hong, S. Ju, Y. Yang, J. Zheng, G. Xia, Z. Huang, X. Liu, X. Yu, Hollow-shell structured porous $CoSe_2$ microspheres encapsulated by MXene nanosheets for advanced lithium storage, Sustain. Energy Fuels 4 (2020) 2352–2362.

[43] X. Sun, K. Tan, Y. Liu, J. Zhang, D.K. Denis, Fu Zaman, L. Hou, C. Yuan, A two-dimensional assembly of ultrafine cobalt oxide nanocrystallites anchored on single-layer $Ti_3C_2T_x$ nanosheets with enhanced lithium storage for Li-ion batteries, Nanoscale 11 (2019) 16755–16766.

[44] X. Li, Z. Ao, J. Liu, H. Sun, A.I. Rykov, J. Wang, Topotactic transformation of metal-organic frameworks to graphene-encapsulated transition-metal nitrides as efficient Fenton-like catalysts, ACS Nano 10 (2016) 11532–11540.

[45] Y. Liu, R. Luo, Y. Li, J. Qi, C. Wang, J. Li, X. Sun, L. Wang, Sandwich-like Co_3O_4/MXene composite with enhanced catalytic performance for bisphenol A degradation, Chem. Eng. J. 347 (2018) 731–740.

[46] F. Wang, Y. Lai, Q. Fang, Z. Li, P. Ou, W. Wu, Y. Duan, Z. Chen, S. Li, Y. Zhang, Facile fabricate of novel Co(OH)F@MXenes catalysts and their catalytic activity on bisphenol A by peroxymonosulfate activation: The reaction kinetics and mechanism, Appl. Catal. B Environ. 262 (2020), 118099.

[47] Y. Li, T. Yang, S. Qiu, W. Lin, J. Yan, S. Fan, Q. Zhou, Uniform N-coordinated single-atomic iron sites dispersed in porous carbon framework to activate PMS for efficient BPA degradation via high-valent iron-oxo species, Chem. Eng. J. 389 (2020), 124382.

[48] X. Li, Z. Wang, B. Zhang, A.I. Rykov, M.A. Ahmed, J. Wang, $Fe_xCo_{3-x}O_4$ nanocages derived from nanoscale metal-organic frameworks for removal of bisphenol A by activation of peroxymonosulfate, Appl. Catal. B Environ. 181 (2016) 788–799.

[49] Y. Wang, D. Cao, M. Liu, X. Zhao, Insights into heterogeneous catalytic activation of peroxymonosulfate by Pd/g-C_3N_4: the role of superoxide radical and singlet oxygen, Catal. Commun. 102 (2017) 85–88.

[50] X. Li, A.I. Rykov, B. Zhang, Y. Zhang, J. Wang, Graphene encapsulated Fe_xCo_y nanocages derived from metal-organic frameworks as efficient activators for peroxymonosulfate, Catal. Sci. Technol. 6 (2016) 7486–7494.

[51] Y. Qi, J. Li, Y. Zhang, Q. Cao, Y. Si, Z. Wu, M. Akram, X. Xu, Novel lignin-based single atom catalysts as peroxymonosulfate activator for pollutants degradation: Role of single cobalt and electron transfer pathway, Appl. Catal. B Environ. 286 (2021), 119910.

[52] H. Fu, H. Luo, Q. Lin, Q. Zhong, Z. Huang, Y. Wang, L. Wu, Transformation to nonradical pathway for the activation of peroxydisulfate after doping S into Fe_3C-encapsulated N/S-codoped carbon nanotubes, Chem. Eng. J. 409 (2021), 128201.

[53] H. Wang, W. Guo, B. Liu, Q. Si, H. Luo, Q. Zhao, N. Ren, Sludge-derived biochar as efficient persulfate activators: Sulfurization-induced electronic structure modulation and disparate nonradical mechanisms, Appl. Catal. B Environ. 279 (2020), 119361.

[54] T. Yang, S. Fan, Y. Li, Q. Zhou, Fe-N/C single-atom catalysts with high density of Fe-N_x sites toward peroxymonosulfate activation for high-efficient oxidation of bisphenol A: electron-transfer mechanism, Chem. Eng. J. 419 (2021), 129590.

[55] C. Chen, C. Jiang, W. Cao, H. Zhou, Y. Wang, Insight into the difference in activation of peroxymonosulfate with nitrogen-doped and non-doped carbon catalysts to degrade bisphenol A, J. Environ. Chem. Eng 9 (2021), 105492.

[56] X. Dong, B. Ren, Z. Sun, C. Li, X. Zhang, M. Kong, S. Zheng, D.D. Dionysiou, Monodispersed $CuFe_2O_4$ nanoparticles anchored on natural kaolinite as highly efficient peroxymonosulfate catalyst for bisphenol A degradation, Appl. Catal. B Environ. 253 (2019) 206–217.

[57] A. Fayyaz, K. Saravanakumar, K. Talukdar, Y. Kim, Y. Yoon, C.M. Park, Catalytic oxidation of naproxen in cobalt spinel ferrite decorated $Ti_3C_2T_x$ MXene activated persulfate system: mechanisms and pathways, Chem. Eng. J. 407 (2021), 127842.

[58] H. Song, D. Zu, C. Li, R. Zhou, Y. Wang, W. Zhang, S. Pan, Y. Cai, Z. Li, Y. Shen, J. Ma, Ultrafast activation of peroxymonosulfate by reduction of trace Fe^{3+} with Ti_3C_2 MXene under neutral and alkaline conditions: reducibility and confinement effect, Chem. Eng. J. 423 (2021), 130012.

[59] J. Ruan, M. Zhang, W. Shao, H. Bo, Z. Chen, L. Xu, Z. Chen, C. Gu, W. Qiao, Tailored design of MXene-like 2D MOF derived carbon/Fe_3O_4 Fenton-like catalysts towards effective removal of contaminants via size-exclusion effect, Sep. Purif. Technol. 299 (2022), 121694.

[60] H. Li, C. Shan, B. Pan, Fe(III)-doped g-C_3N_4 mediated peroxymonosulfate activation for selective degradation of phenolic compounds via high-valent iron-oxo species, Environ. Sci. Technol. 52 (2018) 2197–2205.

[61] N. Li, R. Li, X. Duan, B. Yan, W. Liu, Z. Cheng, G. Chen, L. Hou, S. Wang, Correlation of active sites to generated reactive species and degradation routes of organics in peroxymonosulfate activation by Co-loaded carbon, Environ. Sci. Technol. 55 (2021) 16163–16174.

[62] R. Luo, M. Li, C. Wang, M. Zhang, M.A. Nasir Khan, X. Sun, J. Shen, W. Han, L. Wang, J. Li, Singlet oxygen-dominated non-radical oxidation process for efficient degradation of bisphenol A under high salinity condition, Water Res. 148 (2019) 416–424.

[63] Y. Zhao, L. Yu, C. Song, Z. Chen, F. Meng, M. Song, Selective degradation of electron-rich organic pollutants induced by CuO@biochar: The key role of outer-sphere interaction and singlet oxygen, Environ. Sci. Technol. 56 (2022) 10710–10720.

[64] M.L. Farquhar, J.M. Charnock, F.R. Livens, D.J. Vaughan, Mechanisms of arsenic uptake from aqueous solution by interaction with goethite, lepidocrocite, mackinawite, and pyrite: an X-ray absorption spectroscopy study, Environ. Sci. Technol. 36 (2002) 1757–1762.

[65] K.F. Hayes, A.L. Roe, G.E. Brown, K.O. Hodgson, J.O. Leckie, G.A. Parks, In situ X-ray absorption study of surface complexes: selenium oxyanions on α-FeOOH, Science 238 (1987) 783–786.

[66] T. Zhang, H. Zhu, J.P. Croué, Production of sulfate radical from peroxymonosulfate induced by a magnetically separable CuFe$_2$O$_4$ spinel in water: efficiency, stability, and mechanism, Environ. Sci. Technol. 47 (2013) 2784–2791.

[67] S. Zhu, X. Huang, F. Ma, L. Wang, X. Duan, S. Wang, Catalytic removal of aqueous contaminants on N-doped graphitic biochars: Inherent roles of adsorption and nonradical mechanisms, Environ. Sci. Technol. 52 (2018) 8649–8658.

[68] M. Wang, Y. Cui, H. Cao, P. Wei, C. Chen, X. Li, J. Xu, G. Sheng, Activating peroxydisulfate with Co$_3$O$_4$/NiCo$_2$O$_4$ double-shelled nanocages to selectively degrade bisphenol A – a nonradical oxidation process, Appl. Catal. B: Environ. 282 (2021) 119585.

[69] W. Ren, L. Xiong, X. Yuan, Z. Yu, H. Zhang, X. Duan, S. Wang, Activation of peroxydisulfate on carbon nanotubes: electron-transfer mechanism, Environ. Sci. Technol. 53 (2019) 14595–14603.

[70] F. Chen, L. Liu, J. Chen, W. Li, Y. Chen, Y. Zhang, J. Wu, S. Mei, Q. Yang, H. Yu, Efficient decontamination of organic pollutants under high salinity conditions by a nonradical peroxymonosulfate activation system, Water Res. 191 (2021), 116799.

[71] X. Li, Y. Fang, X. Lin, M. Tian, X. An, Y. Fu, R. Li, J. Jin, J. Ma, MOF derived Co$_3$O$_4$ nanoparticles embedded in N-doped mesoporous carbon layer/MWCNT hybrids:

extraordinary bi-functional electrocatalysts for OER and ORR, J. Mater. Chem. A 3 (2015) 17392–17402.

[72] H. Zhang, C. Wang, X. Li, J. Xie, X. Yan, J. Qi, X. Sun, J. Li, Converting mesoporous polydopamine coated MIL-125 (Ti) to a core-shell heterostructure for efficient water desalination, Environ. Sci. Nano 8 (2021) 3536–3545.

[73] X. Duan, W. Tian, H. Zhang, H. Sun, Z. Ao, Z. Shao, S. Wang, sp^2/sp^3 framework from diamond nanocrystals: A key bridge of carbonaceous structure to carbocatalysis, ACS Catal. 9 (2019) 7494–7519.

[74] Y. Gao, Y.S. Zhou, J.B. Park, H. Wang, X.N. He, H.F. Luo, L. Jiang, Y.F. Lu, Resonant excitation of precursor molecules in improving the particle crystallinity, growth rate and optical limiting performance of carbon nano-onions, Nanotechnology 22 (2011), 165604.

[75] P. Shao, P. Jing, X. Duan, H. Lin, L. Yang, W. Ren, F. Deng, B. Li, X. Luo, S. Wang, Revisiting the graphitized nanodiamond-mediated activation of peroxymonosulfate: singlet oxygenation versus electron transfer, Environ. Sci. Technol. 55 (2021) 16078–16087.

[76] P. Zhang, Y. Yang, X. Duan, Y. Liu, S. Wang, Density functional theory calculations for insight into the heterocatalyst reactivity and mechanism in persulfate-based advanced oxidation reactions, ACS Catal. 11 (2021) 11129–11159.

[77] Y. Gao, S. Pang, J. Jiang, J. Ma, Y. Zhou, J. Li, L. Wang, X. Lu, L. Yuan, Transformation of flame retardant tetrabromobisphenol A by aqueous chlorine and the effect of humic acid, Environ. Sci. Technol. 50 (2016) 9608–9618.

[78] C. Guan, J. Jiang, S. Pang, C. Luo, J. Ma, Y. Zhou, Y. Yang, Oxidation kinetics of bromophenols by nonradical activation of peroxydisulfate in the presence of carbon nanotube and formation of brominated polymeric products, Environ. Sci. Technol. 51 (2017) 10718–10728.

[79] J. Miao, W. Geng, P.J.J. Alvarez, M. Long, 2D N-doped porous carbon derived from polydopamine-coated graphitic carbon nitride for efficient nonradical activation of peroxymonosulfate, Environ. Sci. Technol. 54 (2020) 8473–8481.